

Research on Engineering Structures & Materials



www.jresm.org

Research Article

Experimental investigation into the effect of oil separators on screw chiller noise

Amey Majgaonkar ^{1,2,a}, A. Karthikeyan ^{1,b}, Virendra Bhojwani ^{3,c}, M. ArulMurugan ^{4,d}, J. Jayaprabakar ^{*,1,e}

- ¹Department of Mechanical Engineering, Sathyabama Institute of Science and Technology, Chennai, Tamilnadu, India
- ²Kirloskar Chillers Pvt. Ltd., Satara, Maharashtra, India

Abstract

- ³MITADT University, Loni, Pune, Maharashtra, India
- ⁴Department of Mechanical Engineering, S.A. Engineering College, Chennai, Tamilnadu, India

Article Info

Article History:

Received 26 July 2025 Accepted 20 Oct 2025

Keywords:

Chiller;

Twin screw compressor; Oil separator; Broadband noise; Computational fluid dynamics The discharge gas from the oil injected twin-screw compressor contain refrigerant and oil mixture. The oil must be separated effectively from refrigerant with lowest pressure drop and returned to the compressor for the reliable and efficient chiller operation. An oil separator is used for this purpose. The type and design of the oil separator impact in the discharge gas pressure drop, velocity, turbulence and consequently influences a chiller noise. The influence of discharge piping and oil separator configuration on the twin-screw chiller noise are studied using Computational Fluid Dynamics (CFD) modelling and by performing experiments. The oil separator design and double outlet discharge piping contributes in the noise reduction of 2.1 dB(A) at full (100%) load and 1.6 dB(A) at part (50%) load respectively. The design also reduces the pressure drop and improves the oil separation efficiency. Splitting the screw compressor discharge gas contributes in noise reduction and has potential to reduce the overall cost.

© 2025 MIM Research Group. All rights reserved.

1. Introduction

The HVAC and R industry need compact [1], energy efficient and quieter products. Noise control is needed for human comfort, meeting regulations, and improve environment around the equipment. Screw chillers are used in industrial, commercial and Naval HVAC and R applications. The noise generated in a twin-screw compressor depends upon the screw profile, number of lobes, built in volume ratio, pressure pulsation, rotational speed, clearances, mechanical vibrations, discharge port design and oil and liquid injection configuration [2, 3]. Twin-screw compressors noise has fundamental harmonic due to gas pulsation characteristics [4]. A typical twin-screw chiller comprises a screw compressor with two rotors, oil separator, condenser, expansion valve, evaporator and piping. In a chiller, the compressor is primary noise source, and the other components are the secondary noise sources which also impact the overall chiller noise. Thus, the chiller noise is often broadband in nature spreading over a large frequency spectrum in the audible range of the human ear. If the intensity of sound at one or more frequencies is above the adjacent frequencies by more than 5 to 8 dB(A), then such noise feels more annoying to the human ear and known as pure tones. In screw compressors pure tone exist generally at the frequency equals to number of rotor lobes multiplied by the revolutions per second [5]. In twin-screw compressors, the

*Corresponding author: <u>ip21tn@gmail.com</u>

dorcid.org/0000-0002-3082-9296; eorcid.org/0000-0003-3290-5771

DOI: http://dx.doi.org/10.17515/resm2025-1045st0626rs

Res. Eng. Struct. Mat. Vol. x Iss. x (xxxx) xx-xx

refrigerant gas is compressed in the chambers formed by two meshing rotors. The noise control strategy encompasses noise reduction at source and transmission path.

At source the noise is found to reduce as number of lobes increases due to the reduction of the mass flow rate per working volume transferred to discharge chamber causing lower pulsation energy [6]. The compressor designs have been improving to reduce the noise generated at source. The screw compressor manufactures have standardized screw compressor models. Chiller system designers cannot practically modify the compressor model at will as it can change model performance, hence they need to reduce the chiller noise in the transmission path. The methods like using a half-wavelength tube, Helmholtz resonator, and muffler had demonstrated up to 10 dB(A) noise attenuation in transmission path [7–9]. However, these methods produce a surplus pressure drop in discharge line, deteriorating the energy efficiency of chiller and adversely affecting chiller running cost. Helmholtz resonators are only useful for narrowband (tunable to one frequency) whereas screw chillers produce broadband noise. Use of noise absorption materials for the compressor noise jacket [10], pipe valves and fittings [11] and equipment noise enclosures also reduce the noise transmission. However, any additional item increases the capital cost of chiller. Hence, there is a need to find a noise control solution, without adversely affecting fixed and running cost of chiller.

Oil is used screw compressors for lubrication, sealing, absorbing heat of compression, reducing pressure pulsations and operating capacity control slide valve mechanism. The study of oil injection into the twin-screw compressor revealed that the sound pressure levels (SPL) of the fundamental is not influenced by oil, however oil attenuated harmonics [6,12]. The amplitude reduction of the pressure pulsation [12] depends upon the oil injection locations and distribution. A proper design of discharge chamber between the outlet port and connected pipe reduced the sound pressure level in discharge pipe by 5 dB(A) [6]. In practical applications, the oil separator acts like a chamber connecting the screw compressor outlet port to the condenser. The doubleoutlet separator differs from prior studies due to the change in the flow-acoustic field compared with the existing chamber or resonator approaches. This is due to the fact that the existing noise attenuating devices are designed with single outlet connection like the Type A oil separator concept discussed in detail in this paper. In Type A oil separators, the flow remains undivided hence it requires a larger diameter than the Type B oil separator for the same velocity. The oil separator is a pressure vessel. The smaller the diameter of any pressure vessel, the lesser is its weight and cost. Therefore, the Type B oil separator reduces the fixed cost of chiller. An oil separator is an essential part of flooded screw chillers. The influence of oil separator and discharge piping on the twin-screw chiller noise is investigated using CFD modelling and by performing experiments. The design contributes in the chiller noise and discharge pressure drop reduction at lower cost.

2. Concept, Design and Prototype

The gravity settling and demister separation are the design principles used for both the oil separator concepts.

2.1. Concept

This study investigates two concepts of external horizontal oil separators: a conventional single outlet oil separator (Type A) and a novel double outlet oil separator (Type B). The internal configuration of Type A and Type B oil separators is shown Figure 1. The oil-gas mixture enters Type A oil separator at one end and refrigerant gas discharges out from opposite end. The oil-gas mixture enters Type B oil separator at center and refrigerant gas discharges out from the both ends. The outlet pipes also used as support to mount the oil separator over condenser shell and thereby eliminating the dedicated saddle supports needed. Oil is settled in oil pool at bottom from where it is drained. The flow splitting decreases the diameter and cost of Type B oil separator than Type A oil separator. Its impact on the separation efficiency, pressure drop and noise are studied.

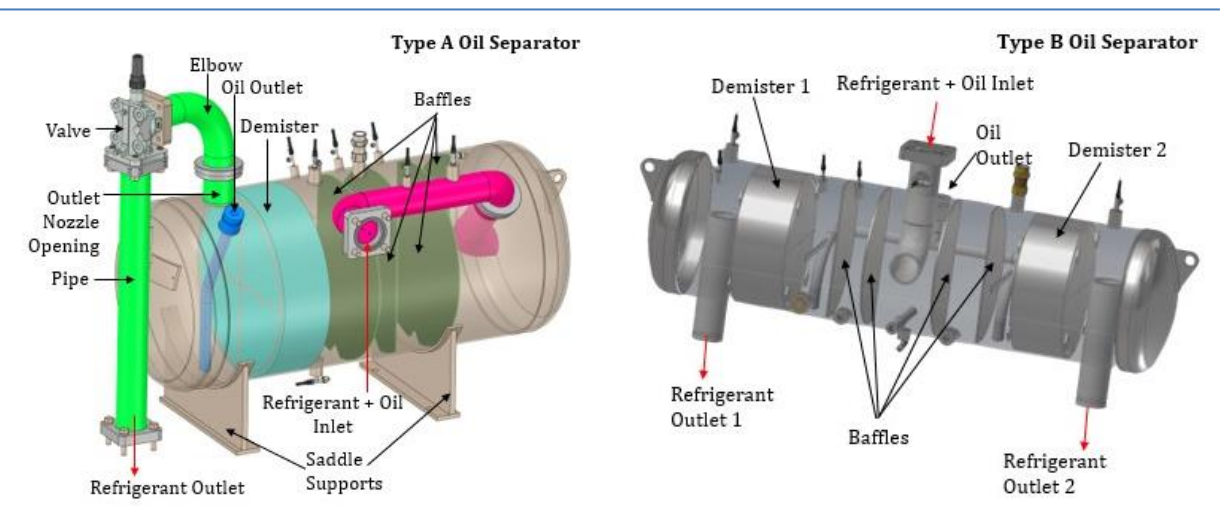


Fig. 1. Internal configuration of oil separators

2.2. Design and Geometry

The normalized simplified geometry of oil separators with discharge piping is illustrated in Figure 2. The Type B oil separator is 33 % lighter in weight compared with the Type A oil separator. Size and weight reduction of oil separator, discharge piping and saddle support elimination with Type B oil separator have potential to reduce cost.

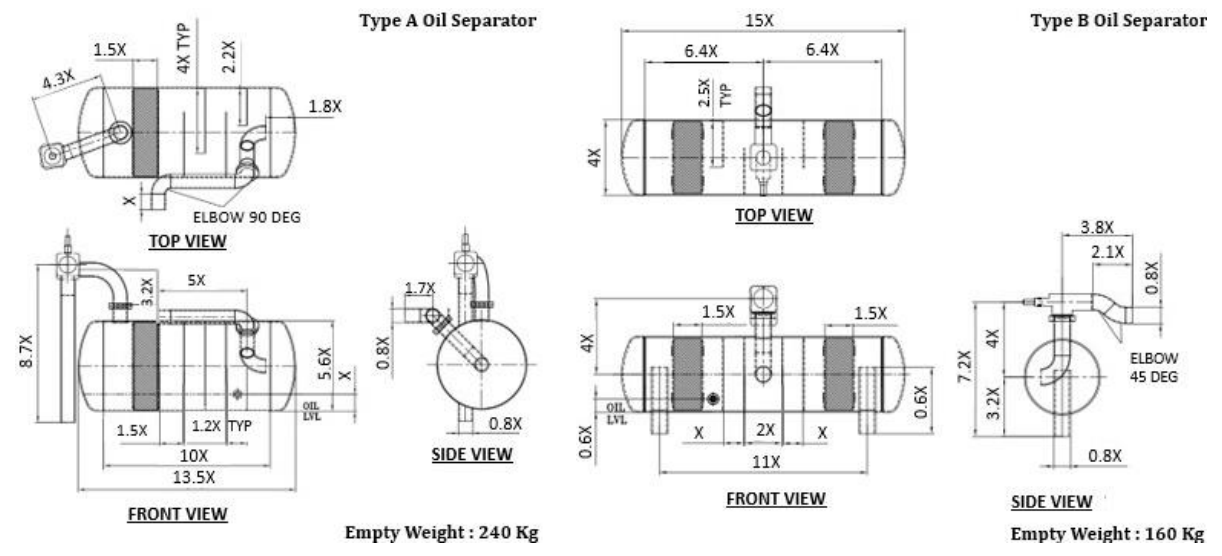


Fig. 2. Geometry of oil separators

2.3 Prototypes

Chiller with Type A oil separator is referred as Type A chiller. Chiller with Type B oil separator is referred Type B chiller. The photographs of Type A and Type B chiller prototypes are shown in Figure 3.

3. CFD Modelling

The CFD analysis is done in the ANSYS Fluent 2020 R2. Discrete phase modeling approach is used as the dispersed oil droplets occupy a low (0.3 %) volume fraction in the refrigerant vapor in line with the previous similar studies [13–18]. The flow is turbulent inside the oil separator and piping as the Reynolds number is high (Re > 400000). The realizable K-epsilon (k- ϵ) model is used in simulation as it provides best performance of all the k- ϵ models. The realizable k- ϵ model is a robust general purpose, high-Re turbulence model, especially for swirling, recirculating, separating and industrial flows. It has two transport equations, first for the turbulent kinetic energy (ϵ) and second for the rate of dissipation of turbulent kinetic energy (ϵ). The k- ϵ turbulence model is selected because it provides a good balance between computational efficiency and accuracy for

capturing the flow behavior in this application. The primary focus of this study is on understanding the bulk flow and separation process for the relative comparison of both oil separator geometries. Further for resolving the near wall phenomena the enhanced wall treatment is also used. Therefore, the k- ϵ model, with enhanced wall treatment is well suitable. The k- ω model is low-Re model. It is more sensitive to near-wall effects. The change in turbulence model to the k- ω model may under predict large-scale swirl though it might not significantly affect the simulation results, its extra computational cost is not justified given the specific objectives of this analysis. For computational purpose the inlet is extended for getting the fully developed flow and achieving the simulation stability. Accordingly, uniform flow profile at gas inlet is considered for both cases for relative comparison study. In the steady state simulations, SIMPLE pressure velocity coupling and the second order upwind discretization is used.



Fig. 3. Photographs of Type A and Type B chiller prototypes

Table 1. Oil particle distribution

Oil Particle size (μm)	Relative no of oil particles
1	1
5	10
10	20
25	90
35	125
50	175
75	240
100	300
200	340
300	335
400	325
500	315
600	300
700	290
800	282
900	275
1000	270

The one-way coupling where the continuous phase always impacts the discrete phase is used in the simulations. Discrete phase is introduced in the simulation by using surface injection at the inlet boundary with a fixed flow rate. A mono-dispersed particle distribution is used for this analysis. Particle-wall interaction is modeled using a trap condition to capture deposition. The injection is set as a group of droplets with a specific size flowing at the same velocity. Additionally, a realistic droplet size distribution is assumed as per Table 1 which provides the relative number of oil

particles with respective to droplet diameters from minimum 1 μ m to maximum 1000 μ m for oil separation efficiency calculation. Fitting the Rosin–Rammler distribution results in mean particle diameter 454.7 μ m with spread parameter of 1.355.

The Type A oil separator use 1 number 22" diameter and Type B oil separator use 2 number 16" demisters pad. All the demister pads are made from 0.15 mm diameter thick steel wires woven to form the $220 \, \text{Kg/m}^3$ dense porous structure. The demister pads provide an extra-large wire surface area of $905 \, \text{m}^2/\text{m}^3$ for efficient oil separation and also has more than $97 \, \%$ void space for lower pressure drop. Demister pads do not need any maintenance. The demisters are considered as porous medium with the viscous and the inertial resistance coefficients derived from curve fitting the experimental data of pressure drop vs velocity as shown Figure 4. The demister thickness is $150 \, \text{mm}$. The data was shared by demister pad manufacturer. The viscous and the inertial resistance coefficients used in study are $486707 \, \text{m}^{-2}$ and $439 \, \text{m}^{-1}$ respectively. The discharge valve used in both the discharge piping is $80 \, \text{NB}$, considered fully open in simulation and experiments.

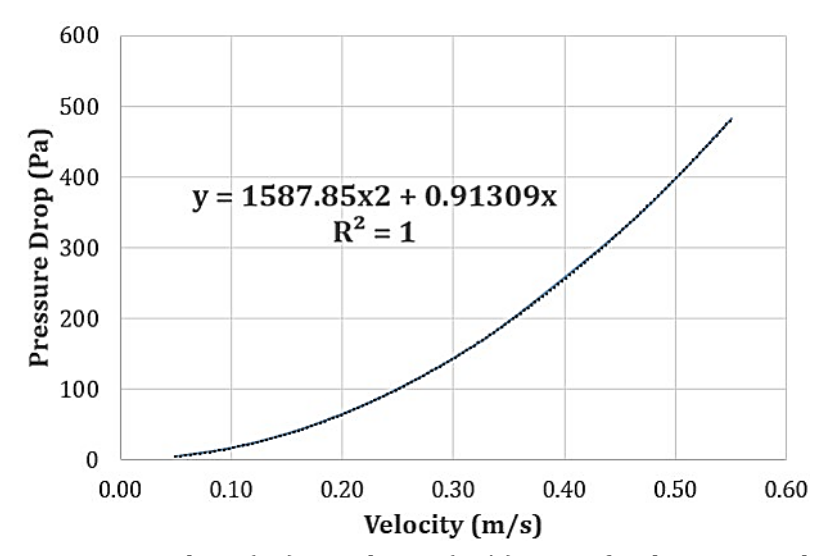


Fig. 4. Pressure drop (Pa) vs velocity (m/s) curve for demister pads

3.1. Governing Equations

3.1.1 Discrete Phase Modeling

The mass conservation equation is

$$\frac{\partial \rho}{\partial t} + \nabla \cdot (\rho \cdot \vec{v}) = S_m \tag{1}$$

In Equation (1) the source ${}^{'}S_{m}{}^{'}$ is the mass added to the continuous phase from the dispersed phase. The momentum conservation equation is

$$\frac{\partial}{\partial t}(\rho \vec{v}) + \nabla \cdot (\rho \vec{v} \ \vec{v}) = -\nabla p + \nabla \cdot (\bar{\tau}) + \rho \vec{g} + \vec{F}$$
 (2)

where, p is the static pressure, \bar{t} is the stress tensor, $\rho \vec{g}$ and \vec{F} are the gravitational body force and external body forces. The stress tensor (\bar{t}) is given by

$$\bar{\bar{\tau}} = \mu \left[\left(\nabla \vec{v} + \nabla \vec{v}^T \right) - \frac{2}{3} \nabla \vec{v} I \right]$$
 (3)

where, μ is the molecular viscosity, $\nabla \vec{v}$ is velocity gradient tensor, $\nabla \vec{v}^T$ is the transpose of the velocity gradient tensor, the unit tensor is I, and the second term on the right-hand side is the effect of volume dilation. The turbulence kinetic energy equation is given by

$$\frac{\partial}{\partial t} (\rho k) + \frac{\partial}{\partial x_i} (\rho k u_j) = \frac{\partial}{\partial x_i} \left[\left(\mu + \frac{\mu_t}{\sigma_k} \right) \frac{\partial k}{\partial x_i} \right] + G_k + G_b - \rho \varepsilon - Y_M + S_k$$
 (4)

where, μ_t is the turbulent viscosity and σ_k is the turbulent Prandtl numbers for k. G_k and G_b denote the turbulence kinetic energies due to the mean velocity gradients and due to buoyancy respectively. Y_M is the contribution of the fluctuating dilatation to the overall dissipation rate. S_k is user defined source term.

$$\frac{\partial}{\partial t} (\rho \varepsilon) + \frac{\partial}{\partial x_i} (\rho \varepsilon u_j) = \frac{\partial}{\partial x_i} \left[\left(\mu + \frac{\mu_t}{\sigma_{\varepsilon}} \right) \frac{\partial \varepsilon}{\partial x_i} \right] + \rho C_1 S_{\varepsilon} - \rho C_2 \frac{\varepsilon^2}{K + \sqrt{\nu \varepsilon}} + C_{1\varepsilon} \frac{\varepsilon}{k} C_{3\varepsilon} G_b + S_{\varepsilon}$$
 (5)

where, σ_{ϵ} is the turbulent Prandtl numbers for ϵ . C_2 , $C_{1\epsilon}$ and $C_{3\epsilon}$ are the constants. S_{ϵ} is user defined source terms.

$$C_1 = Max \left[0.43, \frac{n}{n+5} \right] \tag{6}$$

$$n = S \frac{k}{\varepsilon}$$

$$S = \sqrt{2S_{ij}S_{ij}}$$
(8)

$$S = \sqrt{2S_{ij}S_{ij}} \tag{8}$$

where, S is the mean strain-rate magnitude and Sij is the mean strain-rate tensor. The force balance equation of an oil droplet is given by

$$\frac{d\vec{u}_p}{\partial t} = F_D \left(\vec{u} - \vec{u}_p \right) + \frac{\vec{g} \left(\rho_p - \rho \right)}{\rho_p} + \vec{F}_{\chi} \tag{9}$$

where, the first item on the right-hand side is the drag force per unit particle mass

$$F_{\rm D} = \frac{18\mu}{\rho_n d_p^2} \frac{C_D R_{ep}}{24} \tag{10}$$

where, \vec{u} is fluid phase velocity, \vec{u}_p is particle velocity, μ is the molecular viscosity of the fluid, C_D is the drag coefficient, ρ is the fluid density, ρ_p is the density of the particle and d_p is particle diameter. The Relative Reynolds number Rep calculated as

$$R_{\rm ep} = \frac{\rho d_{\rm p} \left| \vec{u} - \vec{u}_{\rm p} \right|}{u} \tag{11}$$

The constants a₁, a₂ and a₃ are used to derive the drag coefficient C_D as

$$C_D = a_1 + \frac{a_2}{R_{ep}} + \frac{a_3}{R_{ep}2} \tag{12}$$

$$\vec{F}_{x} = \frac{2Kv^{\frac{1}{2}}\rho d_{ij}}{\rho_{p}d_{p}\left(d_{lk}d_{kl}\right)^{\frac{1}{4}}}\left(\vec{u} - \vec{u}_{p}\right) \tag{13}$$

where, K is the empirical drag constant considered as 2.594, d_{ij} is deformation tensor, v is the kinematic viscosity. d_{lk}d_{kl} is the tensor contraction (magnitude of strain rate squared)

3.1.2 Broadband Noise Modelling

The acoustic analysis is conducted using the Broadband noise model, which estimates acoustic sources directly from turbulence parameters. The Proudman's formula provides measure of the local contribution to total acoustic power per unit volume in a given turbulence field. The governing equations based on Proudman's formula for broadband source prediction is

$$P_A = \alpha \rho_0(\frac{u^3}{l})(\frac{u^5}{a_0^5}) \tag{14}$$

Where, P_A is acoustic power, α is a model constant. ρ_0 is mean fluid density. u and l are the turbulence velocity and length scales, respectively, and a_0 is the speed of sound. In terms of k and ϵ the equation (14) becomes

$$P_{A} = \alpha_{\varepsilon} \rho_{0} \varepsilon M_{t}^{5} \tag{15}$$

where, α_{ε} is a constant equal to 0.1. ε is turbulence dissipation rate, M_t is Turbulent Mach number, Lilley's equation for shear noise prediction accounts for the interaction between turbulence and mean shear flow.

$$\frac{\partial^2}{\partial t^2}(p') + 2 U_j \frac{\partial^2 p'}{\partial x_j \partial t} + \left(C_0^2 \delta_{ij} - U_i U_j \right) \frac{\partial^2 p'}{\partial x_i \partial x_j} = \frac{\partial^2 T_{ij}}{\partial x_i \partial x_j}$$
(16)

where, p' is the acoustic pressure perturbation, U_i and U_j are the components of the mean flow velocity vector U in x_i and x_j direction respectively, C_0 is ambient speed of sound, δ_{ij} is Kronecker delta, T_{ij} is Reynold's stress tensor.

The broadband acoustic sources are modeled using Proudman's equation (15) for isotropic turbulence (no shear) and Lilley's equation (16) for shear-noise prediction for calculating acoustic power per unit volume. Integration over the domain gives total acoustic power. The acoustic power in dB, is computed using equation;

$$L_W = 10 \log \left(\frac{P_A}{P_{ref}} \right) \tag{17}$$

where, P_{ref} is the reference acoustic power 10^{-12} W/m³. The broadband noise model is a relative source indicator and not a direct SPL predictor. The broadband noise model provides qualitative source strength; not absolute SPL prediction as Broadband noise model is not designed for far-field prediction. Therefore, direct quantitative comparison of predicted and measured SPL cannot be done. However theoretical formulae are used to convert acoustic power level (APL) to far-field SPL as given below. Equation (17) can be rearranged as;

$$P_A = P_{ref} \ 10^{\frac{L_W}{10}} \tag{18}$$

Equation (19) gives sound intensity assuming spherical spreading in a free-field at a distance r

$$I_S = \frac{P_A}{4\pi r^2} \tag{19}$$

For calculation r = 1 m for equivalent microphone positions. The RMS pressure P' is given in equation (20)

$$P' = (\rho_a \ C_a \ I_s)^{0.5} \tag{20}$$

Where ρ_a is density of air and C_a is sound velocity in air. The SPL is calculated by using the equation (21);

$$L_P = 20\log\left(\frac{P'}{P_{ref}}\right) \tag{21}$$

where, P_{ref} is the reference acoustic power 2 x 10⁻⁵ Pa. The A-weighted SPL is obtained by applying a frequency-dependent correction to the calculated SPL values and compared with microphone measurements, showing agreement within \pm 5.2 dB(A) with heuristic approximation.

3.2. Grid Details

Figure 5 shows the volume mesh representation. T-Grid and Hypermesh are used for grid creation using tetrahedral and prism element types. Five prism layers with a growth rate of 1.2 are applied. This avoids sudden jumps in cell size, which could harm solution accuracy. The aspect ratio is less than 150, ensuring the stretching isn't excessive and skewness is kept below 0.87 and orthogonality is greater than 0.15.

To ensure the grid independent solution the simulations are done by using coarse grid and subsequently with more and more refined grids, until the variation in the in total pressure drop across the oil separator is < 0.03% and almost constant demister face velocity. Refer Figure 6, it is observed that, after 5 million grid sizes, there is no significant change in the converged solution. The grid size of 5.6 million or more is used to eliminate the simulations uncertainty.

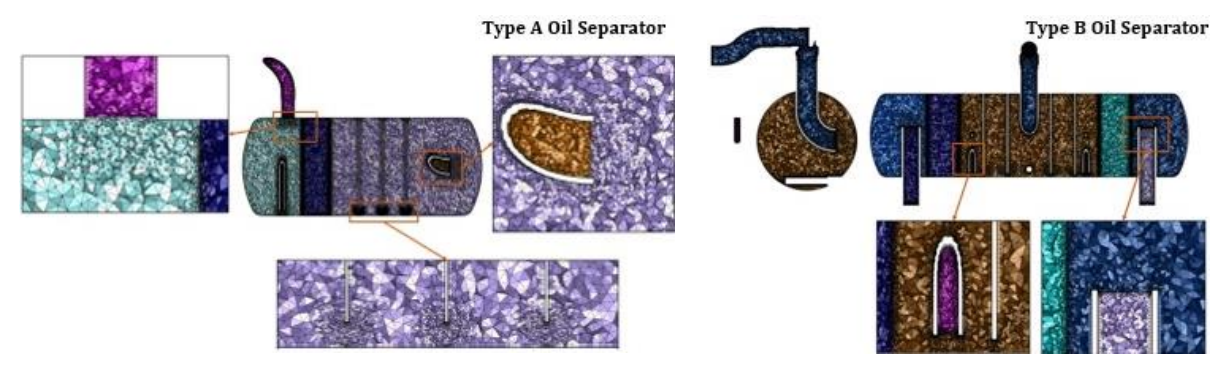


Fig. 5. Representation of volume mesh

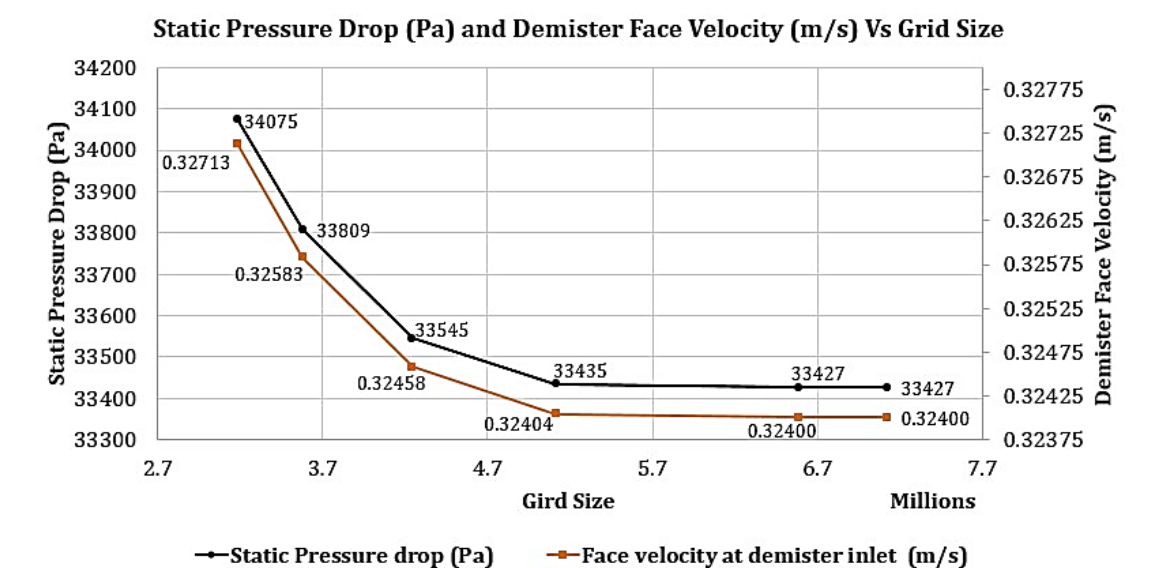


Fig. 6. Graph for grid independent solution

3.3 Near Wall Treatment

The enhanced wall treatment is applied, and target y^+ values are below 300 across all walls. The y^+ value is non-dimensional number which gives judgement about velocity distribution near wall region. The boundary layer effect is captured in CFD by keeping fine grid on wall and first layer thickness of grid is calculated with the help of wall shear stress, Reynold's number and skin friction coefficient as shown below:

$$y^+ = (y * \mu_r)/\nu \tag{22}$$

Where, y is distance from wall, μ_r is Shear Velocity, ν is Kinematic Viscosity

$$\mu_r = \sqrt{\frac{\zeta_w}{\rho}} \tag{23}$$

where, ζ_{ω} is Shear stress, ρ is fluid density.

$$\zeta_{\omega} = \frac{1}{2} C_f \rho u^2 \tag{24}$$

where, Re is Reynold number. C_f is assumed from one-seventh-power law combined with empirical data for turbulent flow through smooth pipes and calculated as

$$C_f = \frac{0.058}{Re^{0.2}} \tag{25}$$

Wall Y plus values on Type A and Type B Oil Separators are given in Figure 7. In both cases the Wall Y plus values is within the range for k epsilon model confirming that the wall effects are captured

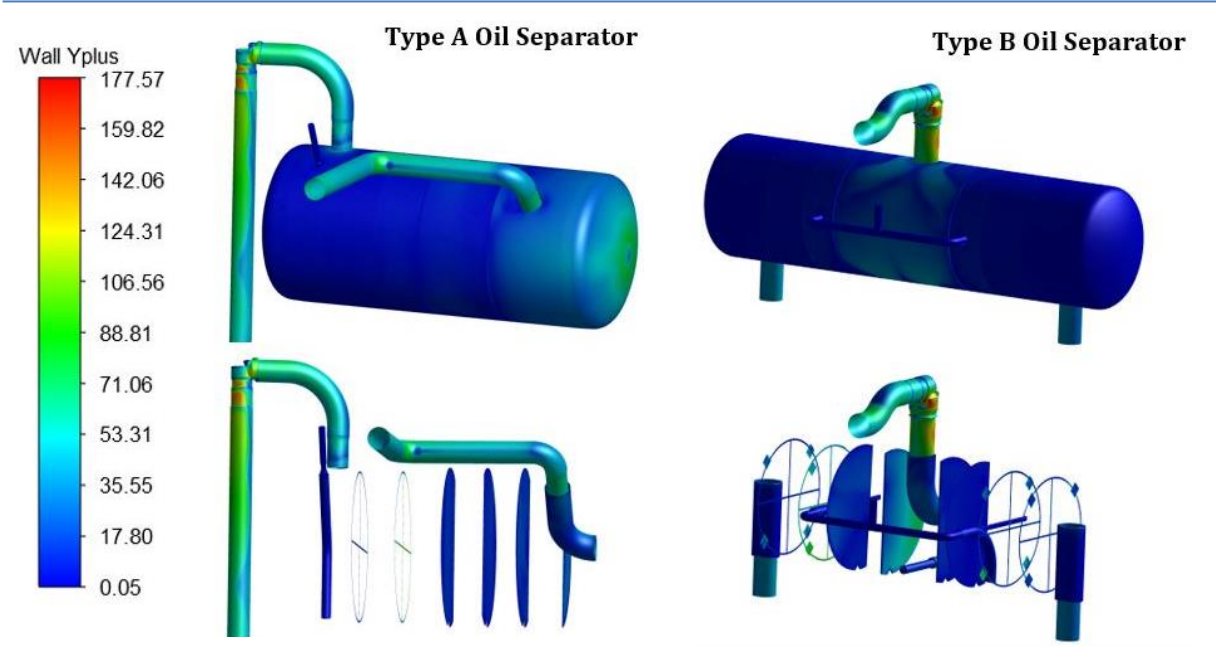


Fig. 7. Wall Y plus for oil separators

3.4 Boundary Conditions

Table 2 informs refrigerant and oil property inputs. Figure 8 shows the boundary conditions used. Table 2. Refrigerant and oil properties

Parameter	Unit	R513a	Oil
Pressure	bar abs	9.66	9.66
Temperature	° C	45.99	45.99
Flow rate	m³/s	0.0765	2.373×10^{-3}
Density	Kg/m ³	48.183	968
Viscosity	Pa-s	12.51×10^{-6}	0.145

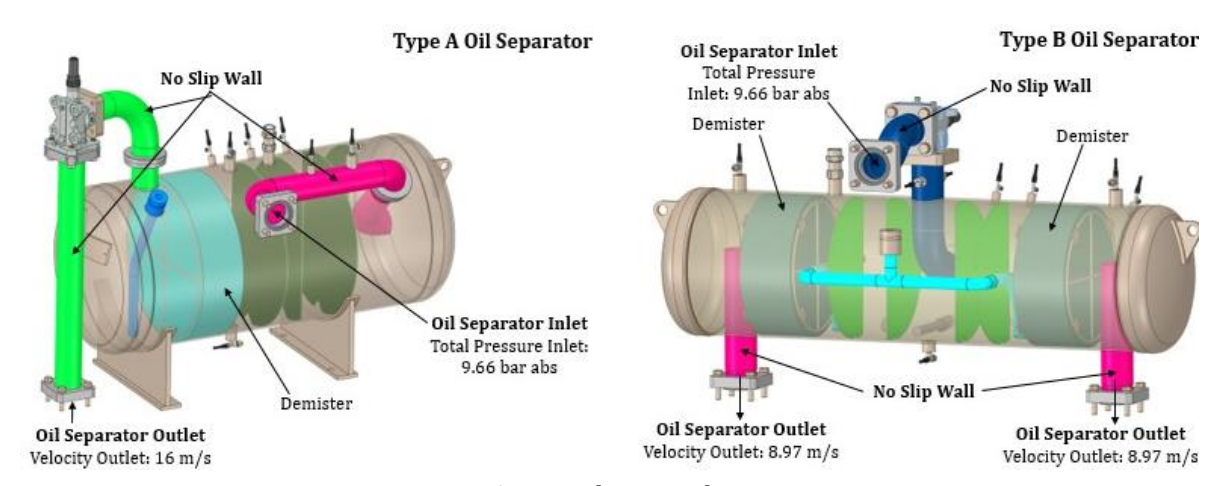


Fig. 8. Boundary conditions

3.5 Post Processing Planes

Figure 9 shows the post processing planes used in the study.

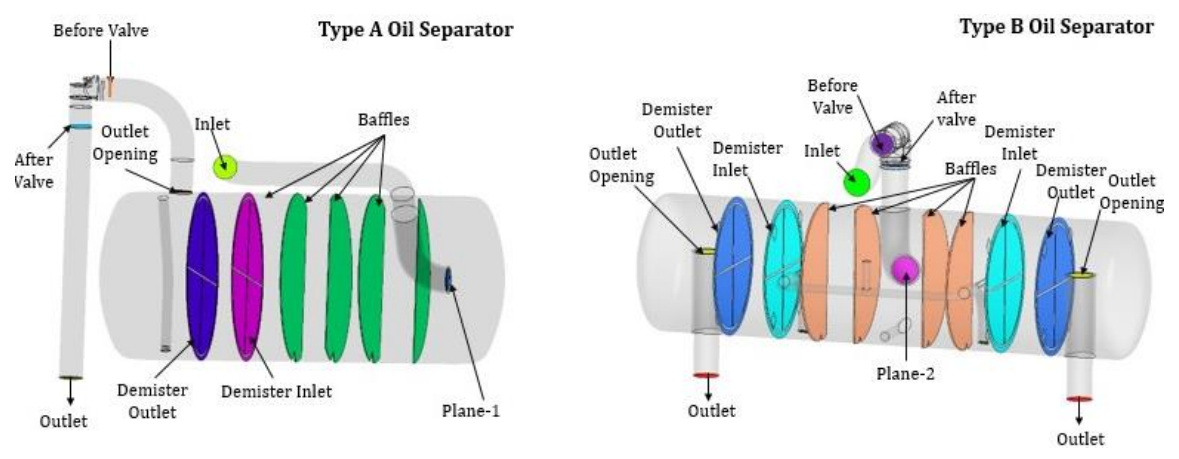


Fig. 9. Post processing planes

3.6 Convergence History

Figure 10 shows the residual plots for Type A and Type B oil separators. Steady residuals indicate that the solutions are converged. This is further confirmed through mass balance.

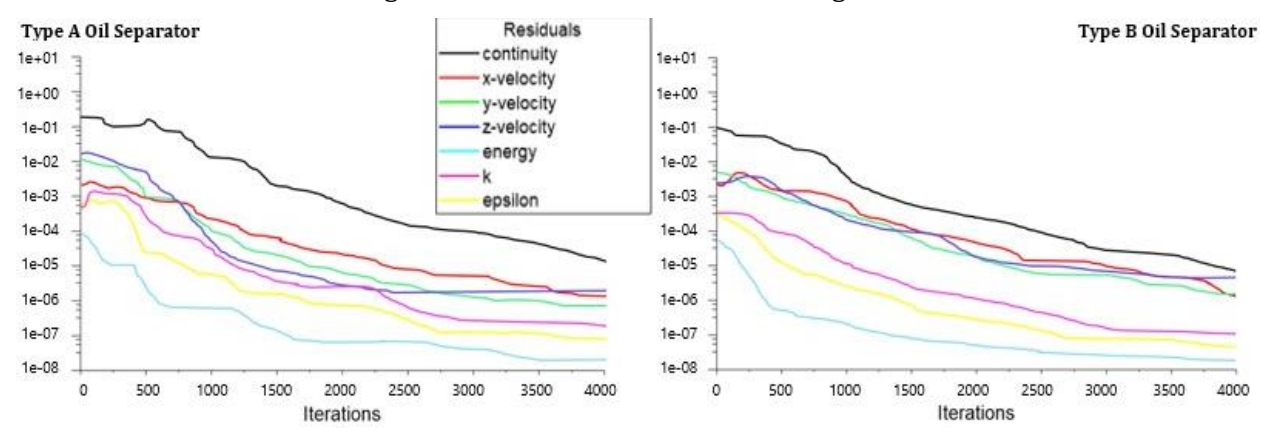


Fig. 10. Residual plots for Type A and Type B oil separators

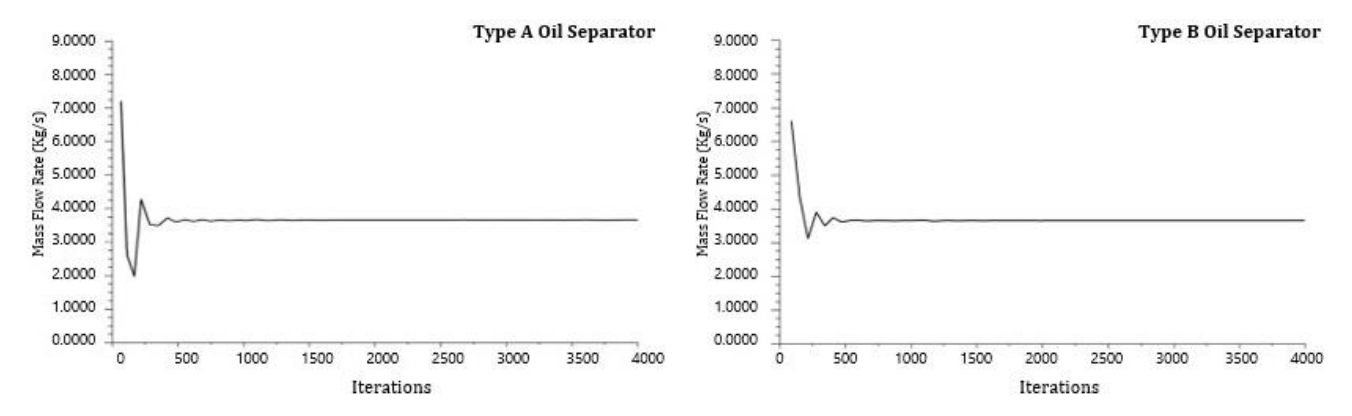


Figure 11. Mass flow rate (kg/s) vs iterations plots for Type A and Type B oil separators

Figure 11 shows the mass flow rate verses iteration plots for Type A and Type B oil separators. No variation in the mass flow rate indicates that the solution is converged. The mass flux report indicates unbalance mass from all inlets to outlets. Since value of this unbalance is close to zero, the convergence of both the models is confirmed.

4. CFD Analysis Results

4.1. Pressure Drop

Table 3 gives the breakup of static and total pressure drop. Negative sign indicates pressure increase.

Table 3. Breakup of static and total pressure drop

Oil Separator:	Γ	Type A		Туре В
Location	Static	Total	Static	Total
	pressure	pressure	pressure	pressure
	drop (Pa)	drop (Pa)	drop (Pa)	drop (Pa)
Inlet to Plane-1	3516	1858	-	-
Inlet to Before Valve	-	-	476	306
Plane-1 or 2 to Demister Inlet	356	7121	(-)89	5511
Demister Inlet to Demister Outlet	167	181	149	157
Demister Outlet to Outlet Opening	11140	1598	2886	366
Outlet Opening to Before valve	(-)1580	2369	-	-
Before Valve to After Valve	24160	16122	19892	16463
After Valve to Outlet	(-)4333	3881	-	-
After Valve to Plane-2	-	-	(-)729	2521
Outlet Opening to Outlet	-	-	(-)364	418
Overall Pressure Drop	33427	33131	22221	25743

Type B oil separator has lower overall pressure drop than Type A due to lower velocity. The contribution of demister pressure drop for Type A and Type B oil separators in the respective overall pressure drop are only 0.5 % to 0.67 %, which is negligible. The CFD computes the pressure drop across the demister pads using inertial and viscous resistance coefficients. These coefficients are derived from pressure drop vs velocity curve (Figure 4) shared by demister pad manufacture as explained in section 3. Since the contribution of demister pressure to the overall pressure drop is itself negligible, the uncertainties in inertial and viscous coefficients calculations also do not affect the simulation results. The shut off valve has highest pressure drop contribution in overall pressure drop in both designs.

4.2. Oil Separation Efficiency

The oil separation efficiency is computed in CFD using monodispersed oil droplet diameters. The oil separation efficiency with respect to oil droplet diameter for Type A and Type B oil separators are plotted in Figure 12. The Type B oil separator has better oil separation efficiency compared with the Type A oil separator for oil droplet diameters up to 35 μm . The oil separation efficiency increases with increase in the oil droplet size and after 35 μm oil droplet diameter it remains constant at 100 % for both the oil separators.

The oil separation efficiency is also computed in CFD using a realistic droplet size distribution as per Table 1. Rosin–Rammler distribution is used to found the mean particle diameter 454.7 μ m with spread parameter of 1.355. With these inputs the CFD computes, the oil separation efficiency as 97.27 % for Type A oil separator and 98.56 % for Type B oil separator.

The velocity of discharge gas plays a very important role in oil separation, pressure drop and also in the acoustic characteristic of an oil separator as it influences turbulence. Figure 13 shows the oil droplet path lines colored by velocity magnitude for 1 to 25 μm oil droplet sizes. As oil droplet size increases the oil droplets trajectories become shorter and they get settled and separated quickly. Beyond 35 μm all oil particles get settled and separated in initial stage only and do not even reach demister hence oil particle trajectories are not shown. As oil droplet size increases, the mass of the oil droplet increases. The bulk amount of oil gets settled by gravity and practically the oil escaping the oil separator is due to the tiny oil particles.

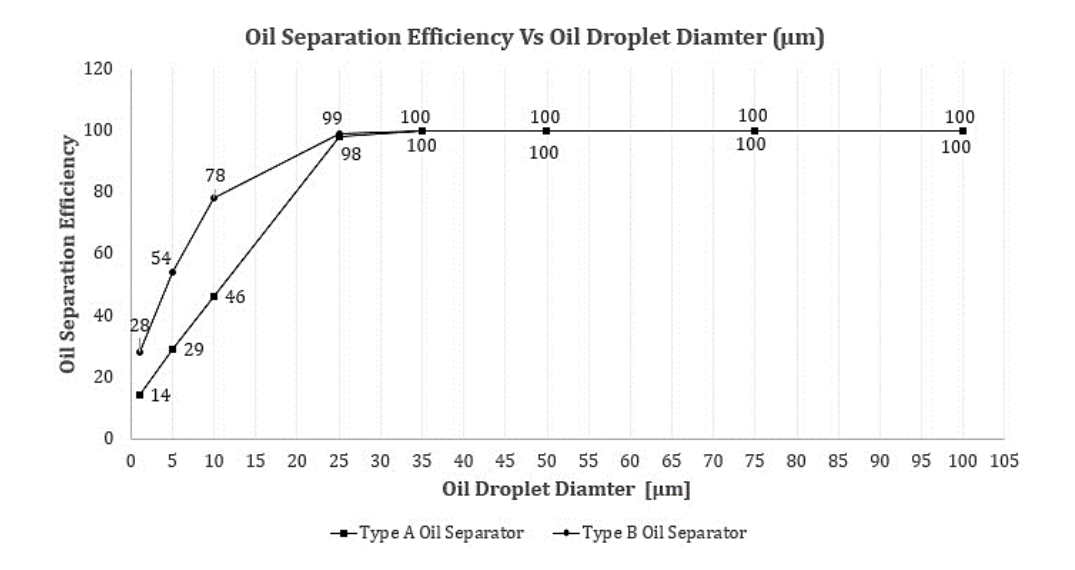


Fig. 12. Oil separation efficiency with mono dispersed oil particle injection

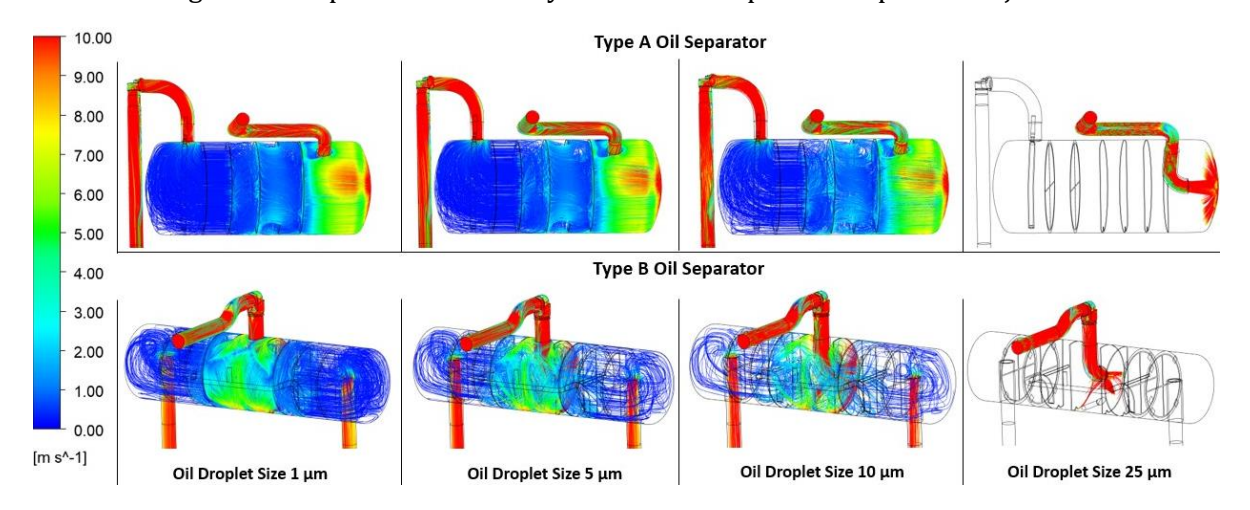


Fig.13. Oil droplet path lines colored by velocity (m/s) magnitude for 1 to 25 μm oil droplets

The velocity distribution and re-entrainment velocity limit for demister governs the oil carry over rate from the demister. Therefore, the velocity distribution on demister surfaces are compared for both the oil separator geometries using the Flow Distribution Index (FDI) calculated using equation

$$FDI = \frac{\int_{A} \left[1 - 0.5 * \left| \frac{V_i - V_{Avg}}{V_{Avg}} \right| \right] dA}{A} \tag{26}$$

Where V_i is local axial velocity through area dA (m/s) and V_{avg} is average axial velocity on corresponding face zone (m/s).

FDI gives the deviation from the average velocity. If the flow is perfectly uniform, the value is close to 1, otherwise it is less than 1. FDI = 0.95 to 1 indicate high uniformity, FDI = 0.9 to 0.95 indicate good uniformity and FDI < 0.9 indicate poor uniformity. It is desirable to have higher values of FDI if average axial velocity is lower than re-entrainment velocity limit. The re-entrainment velocity limit is calculated using the Souders Brown equation

$$V_{max} = K_s * \sqrt{\frac{(\rho_l - \rho_g)}{\rho_g}}$$
 (27)

Where, V_{max} is maximum allowable velocity for the demister (m/s), ρ_l is density of oil (Kg/m³), ρ_g is density of refrigerant vapor (Kg/m³), K_S is system load factor and depends upon application like horizontal or vertical flow, inlet mist load. It is usually 0.11 for SI units. Using the refrigerant and

oil density values from Table 2, the maximum allowable velocity for the demister (m/s) is calculated as 0.481 m/s.

Table 4 gives FDI at demister inlet and outlet for Type A and Type B oil separators. Figure 14 shows the counters of axial velocity on demister and FDI at demister inlet and outlet. Type A and Type B oil separators have average axial velocities as 0.324 m/s and 0.306 m/s respectively, which are sufficiently lower than re-entrainment velocity (0.481 m/s) limit. This confirms that none of the demisters in both the type of oil separators are expected to face the loading and re-entrainment issues. Type B oil separator has lower axial velocity and higher values of FDI compared to that of Type A oil separator. Therefore, Type B oil separator is having better separation efficiency compared to Type A oil separator.

Table 4. FDI at demister inlet and outlet for Type A and Type B oil separators

Oil separator	Type A	Type B	Type B
Demister	1	1	2
FDI at inlet	0.89	0.93	0.94
FDI at outlet	0.89	0.93	0.94

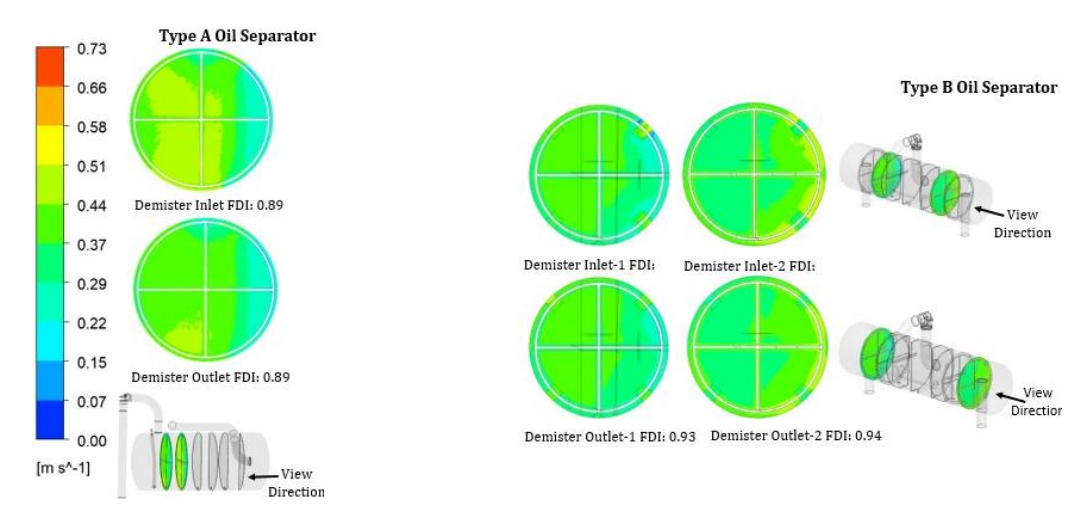


Fig. 14. Counters of axial velocity (m/s) on demister and FDI at demister inlet and outlet

4.3 Turbulence Intensity

The turbulence intensity is defined the ratio of the standard deviation of mean velocity to mean velocity. Figure 15 shows that the contour colored by turbulence intensity on oil separator walls. Type A oil separator has a single outlet connection from which the entire refrigerant flows whereas the Type B oil separator has two outlet connections splitting the refrigerant flow. Splitting the discharge gas in two equal portions and then passing it through respective demisters changes the acoustic flow field. In Type B oil separator, two shorter pipes replace the single longer discharge outlet pipe. All the pipes have same diameter. Therefore, in Type B design the two shorter pipes have lower velocity and related turbulence intensity and turbulence kinetic energy at pipe outlets than Type A design. This indicate that Type A oil separator is more likely to have higher noise than Type B oil separator.

4.4 Turbulence Kinetic Energy

Figure 16 shows the contour colored by the turbulence kinetic energy on the oil separator walls. It can be seen that the Type A oil separator is having higher velocity and higher turbulence kinetic energy than Type B specially at outlet pipes. The turbulent kinetic energy (k) is proportional to square of the mean velocity. In Type A oil separator velocity at outlet pipe is 16 m/s and in Type B oil separator velocity at outlet pipes is 8.97 m/s. That is Type B oil separator has around 56 % lower velocity at outlet than Type A oil separator. The Acoustic power (P_A) varies with turbulent kinetic

energy (k) with a power law. The model dependent coefficient (n_t) value generally varies between 1 to 2 depending upon the model.

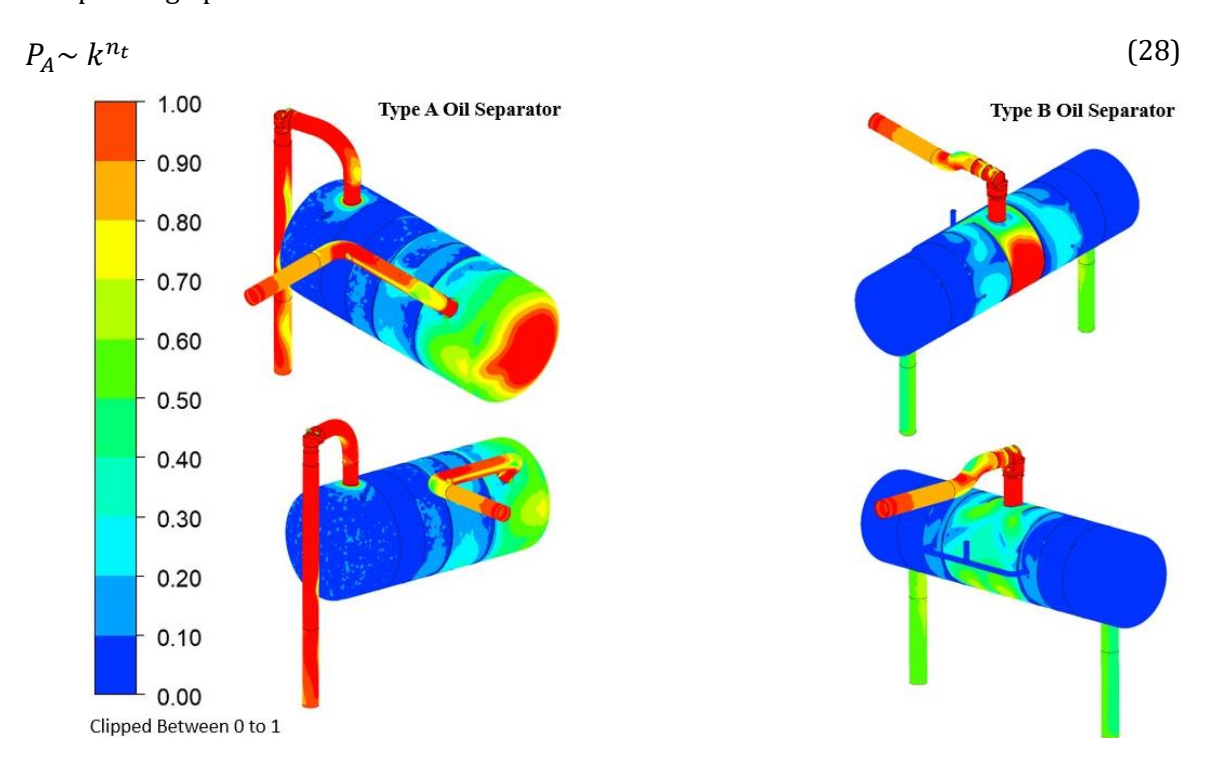


Figure 15. Turbulence intensity on oil separator walls

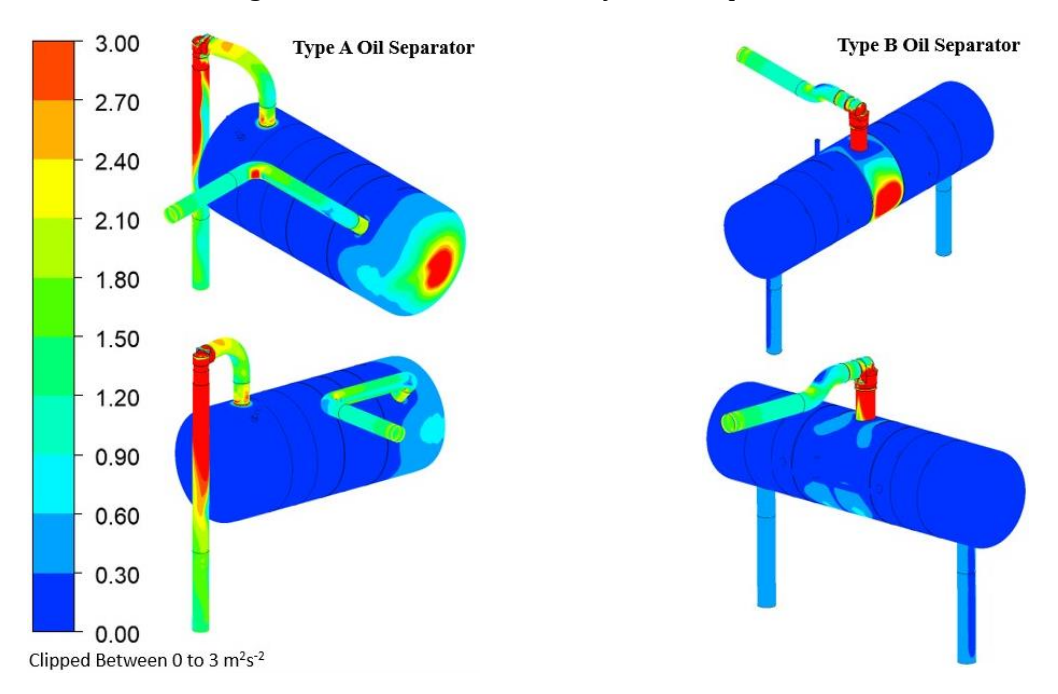


Fig.16. Turbulence kinetic energy (m²/s²) on oil separator walls

Assuming minimum value for model dependent coefficient (n_t =1), there is a reduction of around 5 dB in acoustic power. Therefore, the Type A oil separator is more likely to have higher noise than Type B oil separator.

4.5 Acoustic Power Level

Figure 17 shows acoustic power level contours on oil separator. Inside the oil separators, where the inlet pipe opens and the refrigerant-oil mixture strikes on wall, flow turbulence is generated, causing increased acoustic power level. The Type B design has lower values of acoustic power

levels than Type A design. The smaller area at the valve section creates the flow turbulence, which results in a maximum acoustic power level of around 99.4 dB and 95.9 dB in both Type A and Type B models respectively. The CFD acoustic output is a source indicator rather than a direct prediction.

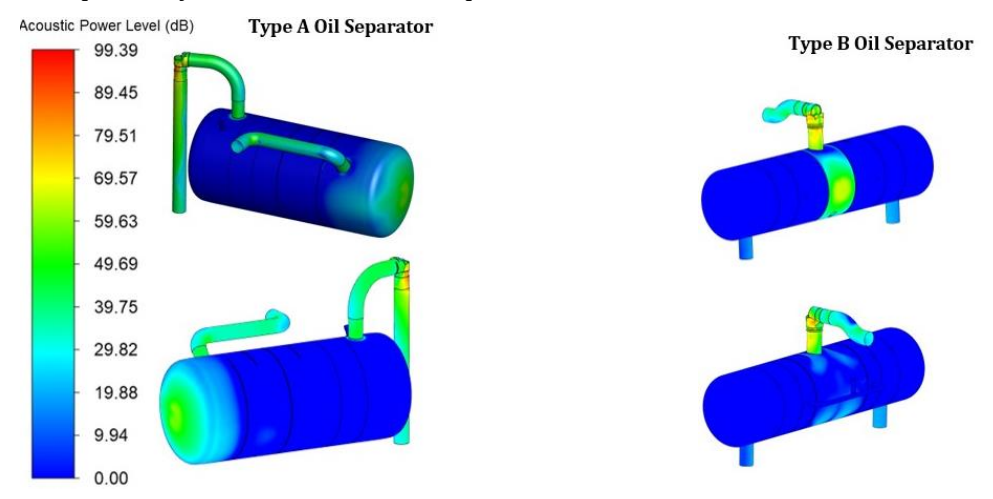


Fig. 17. Acoustic power level (dB) on oil separators

5. Test Set Up, Test Procedure, Test Instruments and Uncertainty Budget

5.1. Pressure Drop and Oil Circulation Rate

Figure 18 shows the experimental set up used for the pressure drop and oil circulation rate (OCR) measurement. The pressure drop is measured across the oil separator for both Type A and Type B chillers. The chillers are tested on the Air-Conditioning, Heating, and Refrigeration Institute (AHRI) approved chiller test bed facility. Both the chillers are tested at same operating points as per AHRI 551/591 (SI) standard [19].

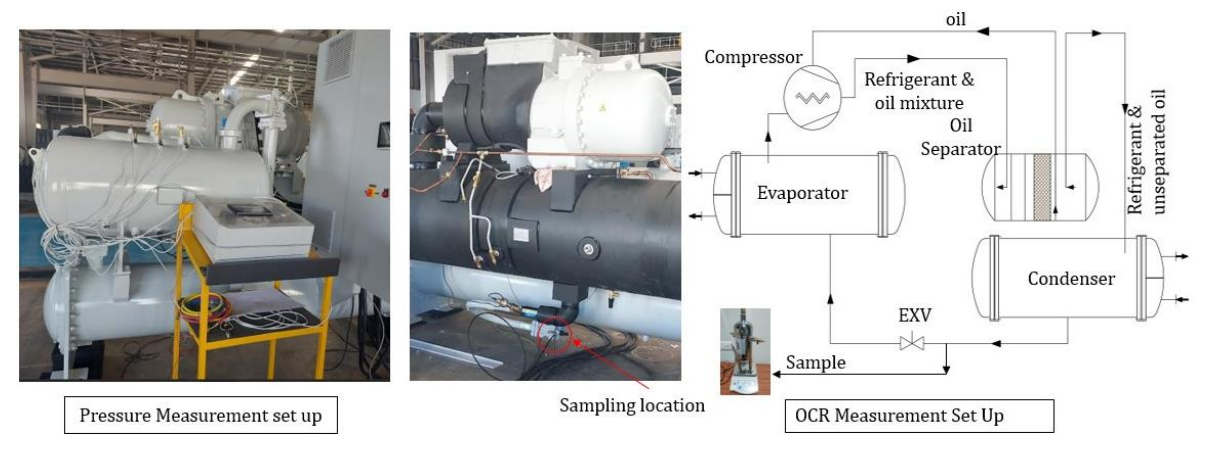


Fig. 18. Experimental set up for pressure drop and oil circulation rate measurement

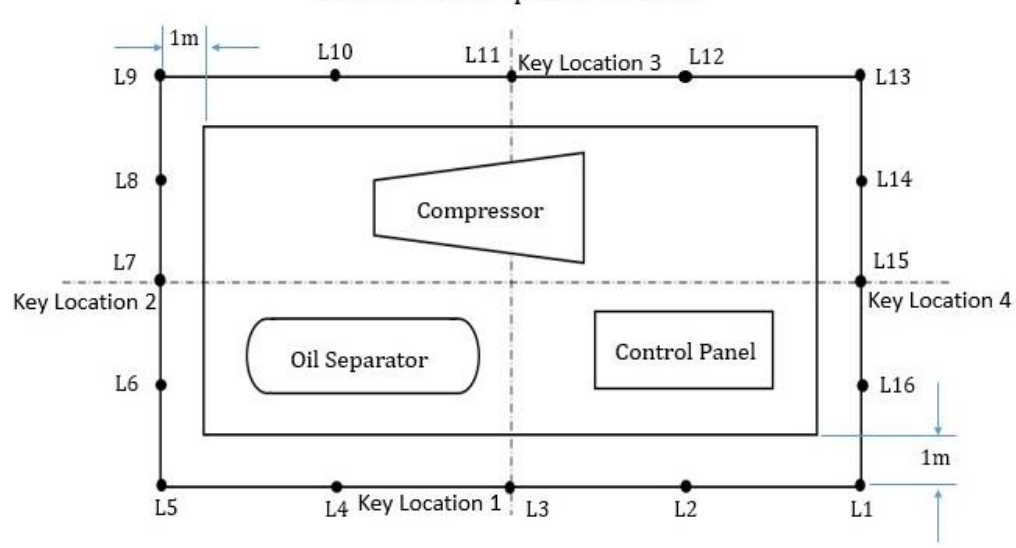
The oil content in refrigerant vapor at outlet of oil separator is negligible on volume basis due to the very high specific volume of refrigerant vapor compared to oil. Hence it is not practical to collect the test sample from the oil separator outlet and measure the oil content in it to find the oil separation efficiency of any oil separator. Therefore, as per ASHRAE 41.4 standard [20] samples of refrigerant and oil mixture are collected after the condenser from the liquid line to measure OCR. The oil percent in sample of refrigerant liquid and oil on mass basis is the OCR. Though OCR is not the exact and instantaneous measure of oil separation inefficiency, it is an indicator accepted in the refrigeration industry. Lower OCR values indicate better oil separation efficiency.

The prototype chillers are extensively tested in the factory at normal and challenging operating conditions including maximum and minimum refrigerant flow rate, low and high lift conditions, low discharge superheat and endurance run. Both chillers successfully passed all the testing

without any oil level trip or performance issues. Both oil separators are reliable and qualified for use. Both oil separators do not need any maintenance.

5.2 Noise

A-weighted sound pressure level (SPL) measured with a reference of 20e-06 Pa in the octave bands from 31 Hz to 8 kHz as per AHRI standard 575 [21]. The measurement points are determined relative to a reference imaginary rectangular parallelepiped that will enclose the machine. Figure 19 shows measurement locations, orientation of test units and key measurement points (L3, L7, L11 and L15). The readings are taken at all the measurement points at a 1 m distance from the chiller periphery and at 1.5 m height from the ground. As per AHRI standard 575, for valid measurement the Sound Pressure Level taken with the test unit operating must be at least 6 dB above the corresponding lev-el with the test unit off and other equipment operating. For each chiller, two complete set of measurements are taken with the test unit operating at full load and the test unit off with all other equipment in the test area operating as before to establish the background sound levels. In both the chillers, the operating noise levels at full load and part (50%) load at all locations are significantly (> 19.9 dB (A)) higher than the background sound levels ensuring no uncertain measurement due to background noise. The atmospheric pressure at test facility is 98 kPa and ambient temperature is 35 Deg C with 60 % relative humidity. Photon+ 4 channel data acquisition system and ICP data acquisition system are used. Microphones used are GRAS make model 46AE with 52 mV/Pa nominal sensitivity, 32 kHz sampling frequency. Average type is linear, 30 Seconds averaging time and time weighting is kept slow.



L1 to L16: Microphone Locations

Fig. 19. Microphone locations with respect to test unit location for SPL measurement

5.3. Details of Measuring Instruments

Table 5 gives complete details of measuring instruments used in the study.

Table 5. Details of measuring instruments

S.N.	Measuring Device and Service	Measured Variable	Range	Resolution / Least Count	Accuracy
1	Evap. water inlet temp sensor (RTD)	Temperature	(-)100 to 157 Deg C	0.0001 Deg C	± 0.1 Deg C
2	Evap. water outlet temp sensor (RTD)	Temperature	(-)100 to 157 Deg C	0.0001 Deg C	± 0.1 Deg C
3	Cond. water inlet temp sensor (RTD)	Temperature	(-)100 to 157 Deg C	0.0001 Deg C	± 0.1 Deg C
4	Cond. water outlet temp sensor (RTD)	Temperature	(-)100 to 157 Deg C	0.0001 Deg C	± 0.1 Deg C
5	Evaporator water flow meter	Water flow	0 to 360 m ³ /hr	1 m³/hr	± 0.5 % of reading

6	Condenser water flow meter	Water flow	0 to 360 m ³ /hr	1 m³/hr	± 0.5 % of reading
7	Power meter (For Voltage)	Voltage	0 to 460 V AC	0.01 V	± 0.5 % of reading
8	Power meter (For Current)	Current	0 to 2500 A AC	0.01 A	± 0.5 % of reading
9	Power meter (For Power)	Power	0 to 1150 kW	0.0001	± 0.5 % of reading
10	Chilled water diff. pressure transducer	Pressure drop	0 to 5 kg/cm ²	0.01 kg/cm ²	± 0.015 kg/cm²
11	Cooling water and Oil Sep. diff. pressure transducer	Pressure drop	0 to 5 kg/cm ²	0.01 kg/cm ²	$\begin{array}{l} \pm \ 0.015 \\ \text{kg/cm}^2 \end{array}$
12	Pressure sensor oil separator inlet	Pressure	0 to 9.3 bar	0.001 bar	1.2% FS
13	Pressure sensor oil separator outlet	Pressure	0 to 9.3 bar	0.001 bar	1.2% FS
14	Noise measurement set up for chiller	SPL	0 to 140 dB(A)	0.01 dB(A)	± 0.25 dB(A)
15	Weighing machine	Weight	0 to 6200 gram	0.01 gram	0.01 gram

5.4. Uncertainty Budget

Table 6 gives expanded uncertainty in each measured variable as per NABL-141 standard [22]. The expanded uncertainty is derived from the combined uncertainty (U_C) calculation based standard uncertainty calculations for uncertainties in repeatability (U_A), calibration certificate(U_1), accuracy (U_2) and resolution (U_3).

Table 6. Uncertainty in measured variables and uncertainty budget

S.N.	Measured Variable	Standard Uncertainty %				confiden coverage	Incertainty (95 % ce level with a e factor k = 2)	
		Ua	U_1	U_2	U_3	Uc	%	Value
1	Evap. water inlet temp.	0.2111	0.0400	0.0577	0.0002	0.2224	± 0.4449	± 0.05 Deg C
2	Evap. water outlet temp.	0.3870	0.0400	0.0577	0.0004	0.3920	± 0.787	± 0.05 Deg C
3	Cond. water inlet temp.	0.0723	0.0400	0.0577	0.0001	0.1008	± 0.2016	± 0.06 Deg C
4	Cond. water outlet temp.	0.0624	0.0400	0.0577	0.0001	0.0939	± 0.1878	± 0.06 Deg C
5	Evap. water flow meter	0.0021	0.0220	0.2887	0.0000	0.2895	± 0.5790	$\pm 0.50 \text{ m}^3/\text{hr}$
6	Condenser water flow	0.0039	0.0220	0.2887	0.0000	0.2895	± 0.5791	\pm 0.60 m ³ /hr
7	Voltage	0.0230	0.1000	0.2887	0.0007	0.2907	± 0.6127	± 2.51 V
8	Current	0.0349	0.0750	0.2887	0.0019	0.3003	± 0.6006	± 0.91 Amps
9	Power	0.1389	0.0650	0.2887	0.0000	0.3269	± 0.6538	$\pm 0.60 \text{ kW}$
10	Chilled water diff. pressure	0.6289	0.0031	0.0087	0.9078	1.1044	± 2.2088	± 0.01 kg/cm ²
11	Cooling water pressure	0.5155	0.0031	0.0087	0.7440	0.9052	± 1.8103	± 0.01 kg/cm ²
12	Pressure Oil Sep. inlet	0.1047	0.2500	0.6928	0.0035	0.7440	<u>+</u> 1.4879	<u>+</u> 0.121 bar
13	Pressure Oil Sep. outlet	0.1212	0.2500	0.6928	0.0037	0.7465	<u>+</u> 1.493	<u>+</u> 0.117 bar
14	Oil Sep. diff. pressure	0.6098	0.0031	0.0087	0.8801	1.0707	± 2.1415	± 0.01 kg/cm ²
15	SPL	0.0254	0.1000	0.5774	0.0036	0.5865	<u>+</u> 1.173	± 0.941 dB(A)
16	Weight	0.0022	0.0000	0.0000	0.0001	0.0022	<u>+</u> 0.0044	<u>+</u> 0.22 gram

6. Experimental Results

6.1. Pressure Drop and Oil Circulation Rate

Table 7 gives the pressure drop and oil circulation rate comparison for oil separators. Figure 20 compares the CFD estimated and experimental pressure drop for the Type A and Type B oil separators. Type A oil separator has higher pressure drop than Type B oil separator in CFD and experiments. The computational and experimental pressure drop values are found to be within 6% range. Type A oil separator has slightly higher oil circulation rates as compared to Type B oil separator as indicated in the CFD estimates.

Table 7. Pressure drop and oil circulation rate comparison for oil separators.

Oil Separator	CFD		Experim	ent	OCR
	Pressure	Flow rate	Pressure drop	Flow rate	
	drop (Pa)	(m ³ /s)	(Pa)	(m ³ /s)	
Type A	33427	0.0765	32500 ± 981	0.07635	0.48
Type B	22221	0.0765	21000 ± 981	0.07662	0.47

Pressure drop comparison CFD vs Experimental 35000 33427 32500 Pressure drop (Pa) 30000 25000 22221 21000 20000 15000 10000 Type A Design Type A Design Type B Design Type B Design CFD estimated Experimentally Experimentally CFD estimated measured measured

Fig. 20. CFD estimated and experimental pressure drop (Pa)

6.2. Noise

Table 8 gives the SPL for the Type A and Type B chillers with respect to the measurement locations at full and part load. The overall noise reduction in Type B chiller is $2.1\ dB(A)$ at full load and $1.6\ dB(A)$ at part load considering maximum noise at all measurement locations.

Table 8. Type A and Type B chiller SPLs with respect to the measurement locations

Measurement	Type A Chiller	Type B Chiller	Type A Chiller	Type B Chiller
Location	Full load	Full load	Part load	Part load
L1	77.1	75.4	70.0	68.3
L2	77.8	75.8	70.6	68.8
L3	80.1	77.4	72.6	70.2
L4	79.7	78.0	73.0	71.3
L5	79.7	77.9	73.4	71.9
L6	79.2	78.0	72.8	71.9
L7	80.4	78.4	73.2	71.2
L8	78.9	77.3	71.7	69.9
L9	79.1	77.2	72.1	70.2
L10	80.1	78.3	73.0	71.3
L11	80.8	78.7	75.3	73.7
L12	78.7	77.1	72.4	70.9

L13	78.2	76.4	72.1	70.4
L14	78.1	76.3	72.5	71.2
L15	78.4	76.8	71.3	70.0
L16	77.8	76.3	69.1	67.7
Maximum	80.8	78.7	75.3	73.7

It is evident from Table 8 that the Type B chiller exhibits lower noise levels across all the measurement locations compared with Type A chiller at full and part load. To reinforce the analysis with statistical confidence, a paired t-test is conducted with null and alternative hypothesis. Null hypothesis, assumes that there is no significant difference in mean noise level between the Type A and Type B chillers. Alternative hypothesis assumes that the mean noise level of Type B chiller is significantly lower than that of the Type A chiller. Table 9 summarizes the paired t-test results for the Type A and Type B chiller noise across all the measurement locations based on readings provided in Table 8.

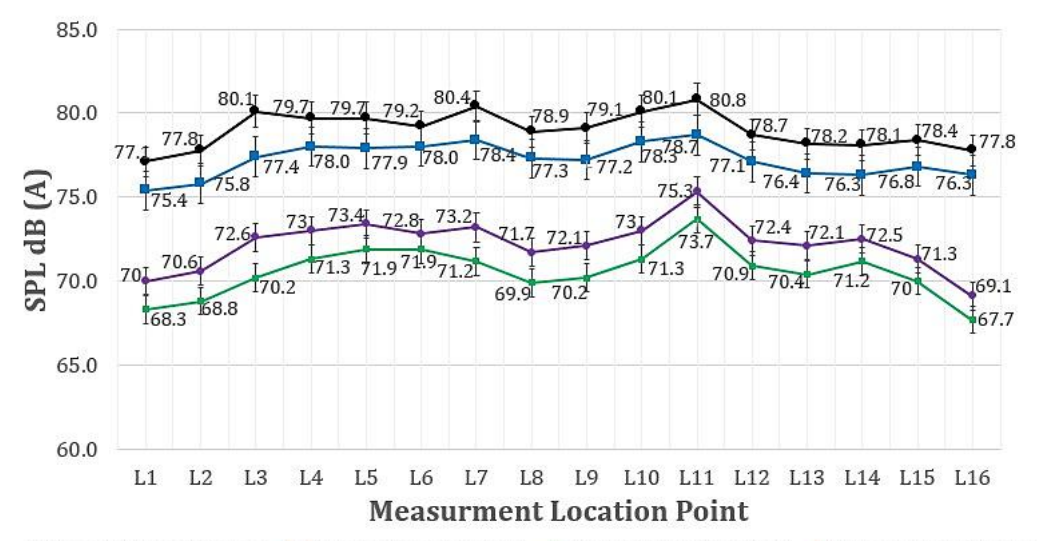
Table 9. Paired t-Test results for the Type A and Type B chiller noise

Chiller	Type A	Type B	Type A	Type B
Load		Full (100 %)		[50 %]
Mean	79.0	77.2	72.2	70.6
Variance	1.1	1.0	2.1	2.2
Observations	16	16	16	16
Pearson Correlation	0.9	95321	0.97364	
Hypothesized Mean		0	0	
Difference				
degrees of freedom (d _f)		15	15	
t-Stat	2	2.18	19.36	
P(T<=t) one-tail	(0.00	0.00	
t Critical one-tail	1.7531		1.7531	
P(T<=t) two-tail	0.000		0.000	
t Critical two-tail	2.1	13145	2.13145	

The calculated t-statistic is compared with a t-critical value ($t_{0.975,15}$) from the t-distribution table at a 95 % confidence level. A p-value below 0.05, rejects the null hypothesis, confirming that the noise reduction achieved by the Type B chiller is statistically significant under both full and part load conditions across all the measurement locations. The overall mean noise reduction for the Type B chiller is 1.8 dB(A) and 1.6 dB(A) at full and part load respectively. Figure 21 shows the SPL for the Type A and Type B chillers with respect to the measurement locations at full and part load in the graphical form. At all measurement locations, both the chillers have higher SPL at full (100%) load than part (50%) load. Both chillers have highest noise at location L11, which is near the compressor. Type A chiller also has higher noise near oil separator outlet at location L7.

Ansys Fluent plots the APL using the broadband noise model. Acoustic power is the energy per unit time radiated as sound. CFD provides only qualitative source estimation rather than actual sound pressure level prediction meaning CFD output is just a source strength, not what a microphone would read. This is a limitation of CFD broadband model. Therefore, direct comparison of CFD output with measurement readings is not appropriate. CFD predicted APLs are 99.4 dB and 95.9 dB for Type A and Type B designs respectively. APLs are converted into the SPLs using equations (18-21) with assumption of distance r as 1 m. The SPL values are 88.5 dB and 85.0 dB for Type A and Type B designs respectively. Assuming that the dominant energy is in the mid-frequency range of 500 Hz, A-weighting corrections of \sim 3.2 dB is applied on both the readings. Thus, APL of 99.4 dB and 95.9 dB gets converted into 85.3 dB(A) and 81.8 dB (A) for Type A and Type B designs respectively with heuristic approximation. This theoretical conversion of APL to SPL is rough approximation and not to be considered for a direct validation. Table 10 gives an indicative comparison of estimated and measured SPL values at selected points (L3, L7 and L11). The

indicative estimates show degree of agreement with measured SPL values within 5.2 dB(A) and 4.5 dB(A) for Type A and Type B chillers respectively.



♣Type A Chiller Full Load ♣Type B Chiller Full Load ♣Type A Chiller Part Load ♣Type B Chiller Part Load

Fig. 21. SPL (dB(A)) with respect to measurement location at full and part load

Table 10. Indicative comparison of estimated and measured SPL (dB(A))

Chiller	Estimated SPL at r=1	Measured SPL at L3	Measured SPL at L7	Measured SPL at L11	Maximum deviation
Type A	85.3	80.1	80.4	80.8	5.2
Type B	81.8	77.4	78.4	78.8	4.4

The SPLs of the Type A and Type B chillers with respect to frequency under full and part load conditions are presented in Table 11. It is evident from Table 11 that the Type B chiller exhibits lower noise levels across all the frequencies compared with Type A chiller at full and part load. To reinforce the analysis with statistical confidence, a paired t-test is conducted with null and alternative hypothesis. Null hypothesis, assumes that there is no significant difference in mean noise level between the Type A and Type B chillers. Alternative hypothesis assumes that the mean noise level of Type B chiller is significantly lower than that of the Type A chiller. Table 12 summarizes the paired t-test results for the Type A and Type B chiller noise across all the frequencies based on readings in Table 11.

Table 11. Type A and Type B chiller SPLs with respect frequency at full and part load

Frequency (Hz)	Type A Chiller	Type B Chiller	Type A Chiller	Type B Chiller
	Full Load	Full Load	Part Load	Part Load
31.5	32.1	28.6	29.2	28.3
63	53.2	50.5	49.8	47.8
125	56.7	54.9	51.4	50
250	76.3	73.1	70.2	69.6
500	77.3	74.5	70.1	69.6
1000	74.9	74.8	70.9	70.5
2000	71.9	71.7	67.3	66.1
4000	67.7	65.8	64.6	62.3
8000	58.7	56.2	52.1	51.2

The calculated t-statistic is compared with a t-critical value ($t_{0.975,8}$) from the t-distribution table at a 95 % confidence level. A p-value below 0.05, rejects the null hypothesis, confirming that the noise reduction achieved by the Type B chiller is statistically significant under both full and part load

conditions across all the measurement locations. The overall mean noise reduction for the Type B chiller is 2.1 dB(A) and 1.1 dB(A) at full and part load respectively.

Table 12. Paired t-Test results for the Type A
--

Chiller	Type A	Type B	Type A	Type B		
Load	Full (100 %)		Part (Part (50 %)		
Mean	63.2	61.1	58.4	57.3		
Variance	216.6	234.6	195.7	200.1		
Observations	9	9	9	9		
Pearson Correlation	0.99749		0.99895			
Hypothesized Mean Difference	0		0			
degrees of freedom (d _f)	8			8		
t-Stat	5.10750		5.12569			
P(T<=t) one-tail	0.00046		0.00045			
t Critical one-tail	1.85955		1.85955			
P(T<=t) two-tail	0.00092		0.00090			
t Critical two-tail	2.30600		2.30600			

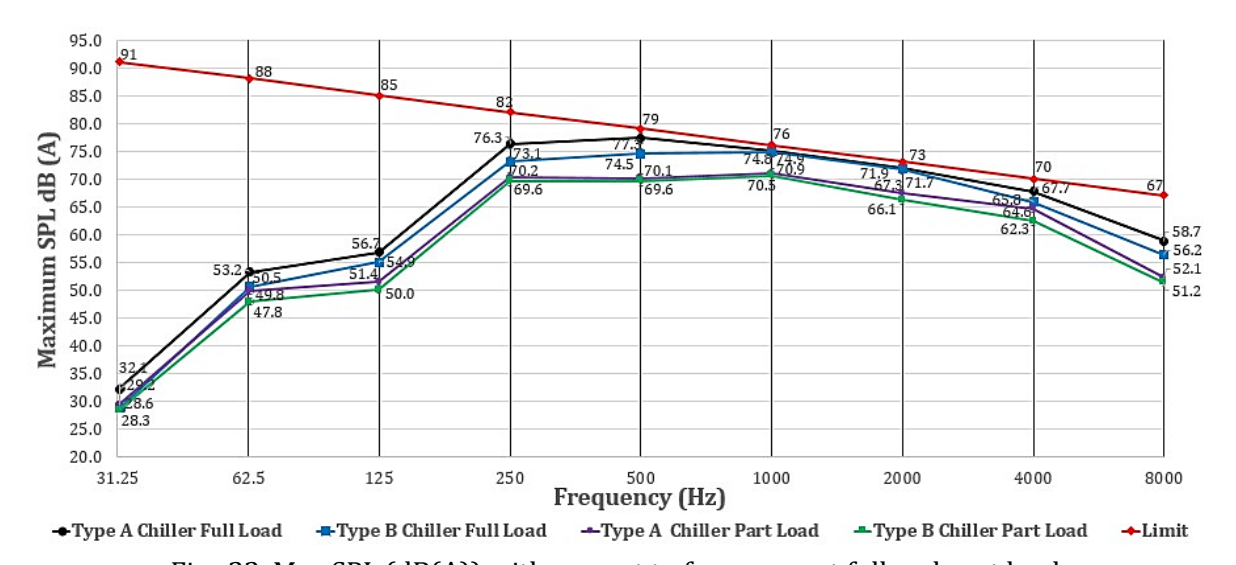


Fig. 22. Max SPL (dB(A)) with respect to frequency at full and part load

Figure 22 shows the maximum SPL measurement with respect to frequency for the Type A and Type B chillers. The readings are also compared against the limits specified in MIL-STD-1474D [23] only as a reference threshold. Both the chillers meet this limits. Both chillers have pure tone noise at 250 Hz frequency. This is due to use of the same compressor in both the chillers which is the main noise source. This is also the reason for L11 to dominate in both the units. At all frequencies, both the chillers have higher SPL at full (100%) load than part (50%) load. Type B chiller has lower SPL compared with Type A chiller at all the measured frequencies at full and part load.

7. Conclusions

The chillers with oil injected twin-screw compressor suffer from noise problems. The noise generated from chillers is broadband in nature. Table 13 summarizes and compare different noise control devices. Traditional devices like using a half-wavelength tube, Helmholtz resonator are effective in reducing the noise in only in certain frequency range and have limited usefulness for broadband noise reduction. The traditional devices like half-wavelength tube, Helmholtz resonator, absorptive muffler and noise jacket are not essential for chiller to function, however these are only required to be used in chiller to control the noise. These items are supplementary requiring additional cost. All the traditional devices (expect external noise jacket) are also responsible for chiller performance degradation due to the additional pressure drop in them. Thus, use of these traditional noise control methods increase chillers fixed and operating cost. Oil

separator is an essential part of the flooded chiller having oil injected twin-screw compressor. The function of an oil separator is to separate the oil from the discharge gas. If sized properly then it also acts as cushioning chamber to suppress the noise. Oil separator and the discharge piping can reduce chiller noise if velocity and associated turbulence is minimized.

Conventional oil separators like Type A oil separator have only one discharge outlet. Therefore, the oil separator internals like demister pad needs to be designed for the entire refrigerant flow rate to keep the velocity across it within the allowable velocity limits. This is necessary to prevent oil carry over. In novel oil separator like Type B oil separator, the refrigerant flow is divided inside the oil separator and directed to flow through two demister pads towards the outlets at both the ends of an oil separator. Therefore, the demister pads need to be designed for the half of the refrigerant flow rate for the same velocity across it. This aids in oil separator cost saving as oil separator diameter and weight is reduced. The Type B oil separator is rested over condenser shell using the outlet pipes without any need for external saddle supports. The diameter of both the outlet pipes is kept same as that of Type A oil separator having single outlet, whereas only half of the entire refrigerant flows through each outlet pipe. Therefore, the velocity and turbulence in Type B oil separator outlet pipes is reduced which helps to reduce the noise.

Table 13. Comparison of noise control devices

Feature	Half- Wavelength Tube	Helmholtz Resonator	Absorbing Muffler	Noise Jacket	Discharge Chamber / Type A Oil Separator	Discharge Chamber / Type B Oil Separator
Principle	Destructive interference by half wavelength	Cavity resonance: mass- spring system absorbs energy	Acoustic absorption by porous materials	Equipment enclosure with sound absorptive material	Sudden expansion to dissipates energy	Sudden expansion and flow split velocity reduction to dissipates energy
Tuning	half wavelength and its odd multiples	One frequency (geometry specific)	Broadband absorption	Not tuned; broadband	Broadband flow- driven	Broadband , flow driven
Frequency Range	Narrowban d targets only specific tone	Extremely narrow- band	Broadband	Broadband (medium- high)	Broadband	Broadband
Best For	Single tonal noise (ducts, fans)	Sharp tonal noise (blade passing, engines)	Fan, blower, jet noise	HVAC item's radiated noise	Discharge gas noise	Discharge gas noise
Pressure Drop	(Baseline + Moderate)	(Baseline + Low)	(Baseline + High)	(Baseline + Zero)	(Base line)	Lower than baseline
Cost	(Baseline + Low)	(Baseline + Low)	(Baseline + High)	(Baseline + Moderate)	(Base line)	lower than baseline
Size	Large for low freq. as wavelength too long	Compact due to small cavity	Bulky due to thick absorptive lining	Compact as it is applied outside the casing	Bulky as large diameter needed	Compact as small diameter needed for split flow

CFD modelling is done to study the influence of oil separator and discharge piping designs on the pressure drop, oil separation efficiency and the twin-screw chiller noise. Both the types of oil separators are manufactured and tested along with the chiller. CFD modelling is found useful in predicting the pressure drop and oil separation efficiency. The CFD computed pressure drop is found to be within 6 % range of experimental pressure drop. The Type B design has lower pressure drop than Type A design at almost equivalent mass flow rate.

In CFD considering monodispersed oil droplets, the oil separation efficiency increases with increase in the oil droplet diameter and then above 35 μm oil droplet diameter it remains constant at 100 % for both the oil separators. Therefore, in CFD the Type B oil separator has equal or better oil separation efficiency than Type A oil separator considering monodispersed oil droplets. Considering realistic oil droplet diameters, oil separation efficiencies for the Type A and Type B oil separator are 97.27 % and 98.56 % respectively. Experimentally the oil circulation rate in chiller with Type B oil separator is slightly lower than chiller with Type A oil separator, indicating better separation efficiency.

The CFD acoustic modeling using broadband noise model helps in comparing the flow-acoustic fields of both the oil separator geometries. The higher velocity in Type A design causes higher turbulence. Therefore, Type A design has higher turbulence intensity, turbulence kinetic energy and also higher values of acoustic power levels than Type B design. The CFD acoustic output is a very good source indicator. Experimentally both the chillers have higher SPL at full (100%) load than part (50%) load at all measurement locations and frequencies. The Type B chiller has lower SPL compared with Type A chiller at all the measured locations and frequencies at full and part load. The Type B oil separator design helps in the noise reduction of 2.1 dB(A) at full load and 1.6 dB(A) at part load respectively. These noise reduction findings are modest but industrially meaningful, especially since they are achieved without additional costly noise-control devices. The noise reduction is seen at all the tested locations and frequencies and validation is provided with statistical confidence using a paired t-tests. Therefore, splitting the discharge flow results in oil separator size, and weight reduction, twin-screw chiller noise reduction and also has a potential for cost reduction.

Acknowledgement

The authors gratefully acknowledge Kirloskar Chillers Pvt. Ltd., India for funding this research and providing access to the manufacturing and test facilities for chillers.

Nomenclature

AHRI: Air-Conditioning, Heating, and Refrigeration Institute

APL: Acoustic Power Level

CFD: Computational Fluid Dynamics

FDI: Flow Distribution Index OCR: Oil Circulation Rate SPL: Sound Pressure Level

References

- [1] Ram, A., Jeyakumar P.D., Doss, P. Variable tube geometry micro channel heat exchanger (MCHX) using analytical and CFD analysis. Journal of Research on Engineering Structures and Materials (RESM), 2025;11(4). https://dx.doi.org/10.17515/resm2025-472an1005rs
- [2] Mujic, E., Kovacevic, A., Stosic, N., Smith, I. Noise generation and suppression in twin screw compressors. Journal of Process Mechanical Engineering, 2011;225(2): 127-148. https://doi.org/10.1177/1464419311403875
- [3] Fujiwara, A., and Sakurai, N. Experimental analysis of screw compressor noise and vibration. Journal of Sound & Vibration, 1986; 28(3): 375-401. https://docs.lib.purdue.edu/icec/553
- [4] Zhilong H., Dantong L, Yaoxiang H., Minglong Z., Ziwen X., Xiaolin W. Noise control of a twin-screw refrigeration compressor. International Journal of Refrigeration. 2021; 124:30-42. https://doi.org/10.1016/j.ijrefrig.2020.12.008
- [5] Paulauskis, J. Addressing noise problems in screw chillers. ASHRAE Journal., 1999; June: 22-25.

- [6] Sangfors, B. Modeling, measurements & analysis of gas-flow generated noise from twin-screw compressors. International Compressor Engineering Conference, Purdue, USA, July, 2000. https://docs.lib.purdue.edu/icec/1487
- [7] Zhilong H., Yaoxiang H., Wenqing C., Minglong Z., Ziwen X. Noise control of a two-stage screw refrigeration compressor. Applied Acoustics. 2020; 167: 107383. https://doi.org/10.1016/j.apacoust.2020.107383
- [8] Sun, S., Ziwen X., Chen, W., Zhou, M., Huang, Y., Chia S. Numerical analysis on a perforated muffler applied in the discharge chamber of a twin screw refrigeration compressor based on fluid-acoustic coupling method. International Compressor Engineering Conference, Purdue, USA, May, 2021. https://docs.lib.purdue.edu/icec/2672
- [9] Shen j., Chen, W., Yan, S., Zhou M., Liu H. Study on the noise reduction methods for a semi-hermetic variable frequency twin-screw refrigeration compressor. International Journal of Refrigeration. 2021; 125:1-12. https://doi.org/10.1016/j.ijrefrig.2020.12.029
- [10] Badini, J., Brown, P. Guidelines for reducing the noise level of a centrifugal air compressor installation. Proceedings of the Second Middle East Turbomachinery Symposium Doha, Qatar, March, 2013.
- [11] ISO 15665. Acoustics-Acoustic insulation for pipes, valves, and flanges. 2003. Geneva, Switzerland, ISO.
- [12] Yang, S., Ouyanga, H., Yadong, W., Wang, L. Experimental study of lubricating oil impact on pressure pulsation for twin-screw refrigeration compressor. International Journal of Refrigeration. 2020; 112: 324-332. https://doi.org/10.1016/j.ijrefrig.2019.12.018
- [13] Laleh, A., Svrcek, W., Monnery, W. Computational fluid dynamics-based study of an oil-field separator-part I: A realistic simulation. Society of Petroleum Engineers, Oil and gas facilities. 2012; 90: 57-68. https://doi.org/10.1002/cjce.20665
- [14] Gaffarkhah, A., Shahrabi, A., Moraveji, M., Eslami, H. Application of CFD for designing conventional three phase oilfield separator. Egyptian Journal of Petroleum, 2017; 26(2):313-420. https://doi.org/10.1016/j.ejpe.2016.06.003
- [15] Oliveira J., Fonte, C., Fontes, C. Numerical simulation of demister equipment for application in gravitational separators. Proceedings of COBEM 2009, 20th International Congress of Mechanical Engineering, Gramado, RS, Brazil, November, 2009.
- [16] Feng, J., Chang, Y., Peng, X., Qu, Z., Investigation of the oil–gas separation in a horizontal separator for oil injected compressor units. Proceedings of the institution of mechanical engineers, part A, Journal of Power and Energy. 2008; 222: 403-412. https://doi.org/10.1243/09576509JPE550
- [17] Zhongyia, W., Changlong, Y., Jia, H. Yunliang, Y. The analysis of internal flow field in oil-gas separator, Procedia Engineering. 2011; 15: 4337-4341. https://doi.org/10.1016/j.proeng.2011.08.814
- [18] Eastwick, C., Hibberd, S., Simmons, K., Wang, Y., Care, I., Aroussi, A. Using CFD to improve aero-engine air/oil separator design. Proceedings of the ASME 2002 Pressure Vessels and Piping Conference. Computational Technologies for Fluid/Thermal/Structural/Chemical Systems with Industrial Applications. Vancouver, BC, Canada, August 2002. https://doi.org/10.1115/PVP2002-1554
- [19] ANSI/AHRI Standard 551/591-2023 (SI), Standard for Performance Rating of Water-chilling and Heat Pump Water-heating Packages Using the Vapor Compression Cycle. 2023. Air-Conditioning, Heating, and Refrigeration Institute
- [20] ASHRAE 41.4. Standard Method for Measurement of Proportion of Lubricant in Liquid Refrigerant. 1996. American Society of Heating, Refrigerating and Air-Conditioning Engineers
- [21] AHRI Standard 575. Method of measuring machinery sound within an equipment space. 2022. Air-Conditioning, Heating, and Refrigeration Institute
- [22] NABL-141 (2). Guidelines for Estimation and Expression of Uncertainty in Measurement. 2000. National Accreditation Board for Testing and Calibration Laboratories India
- [23] MIL-STD-1474D. Noise limits. 1997. U.S. Department of Defense.